Journal of the European Ceramic Society 20 (2000) 751–760

Room and high temperature failure mechanisms in solid oxide fuel cell electrolytes

F.L. Lowrie *, R.D. Rawlings

Imperial College of Science Technology and Medicine, Department of Materials, Prince Consort Road, London SW7 2BP, UK

Received 17 September 1998; accepted 12 March 1999

Abstract

The microstructural stability at elevated temperatures and the mechanical properties of 8 mol% yttria stabilised zirconia (YSZ) has been investigated. The YSZ was supplied by two manufacturers as 150 μm thick sheet suitable for the electrolyte in a planar solid oxide fuel cell (SOFC). The two materials had the cubic structure and this crystal structure was maintained up to 1100°C, which was the highest temperature investigated. However, there were differences, albeit small in most cases, in composition, density, grain size and surface finish between the products from the two manufacturers. Although the compositional and structural variations resulted in some differences in mechanical performance, the general trends shown by both materials were similar. The strength, as determined by biaxial flexure, fell by 23–30% on increasing the test temperature from room temperature (RT) to the SOFC operating temperature of 950°C and there was evidence for changes in crack initiation and propagation mechanisms at the higher temperature. The loading rate dependence of the RT strength yielded a low value for the stress exponent n in the standard lifetime equation, which indicated that sub-critical crack growth (sccg) was sensitive to applied stress. Constant load tests at 950–1000°C illustrated the sensitivity of sccg to stress and revealed that creep was also operative in this temperature range. It was concluded that the creep probably occurred by a grain boundary diffusion mechanism.

Keywords: Creep; Fracture; Fuel cells; ZrO_2; Failure mechanisms

1. Introduction

The solid oxide fuel cell (SOFC) is one system of renewable energy being developed, and is designed to produce electricity from a chemical reaction. The basic unit, or cell, consists of a dense electrolyte, capable of conducting oxygen ions at high temperatures, coated on either side with porous, electrically conducting, electrodes. The particular SOFC design under consideration in this paper is the planar design, shown in Fig. 1.[1] Oxygen ions produced at the cathode diffuse through the electrolyte to the anode, where they react with the fuel, in this case hydrogen, to release electrons (i.e. produce electricity). Many of these cells are stacked together to give a working component known as a stack.

In this design the electrolyte serves two purposes, namely separating and supporting the electrodes. It is important that the gases do not react directly, for example by leaking through the electrolyte, so as well as having an adequate ionic conductivity, the electrolyte must be strong enough to withstand room temperature assembly stresses and be mechanically stable for long periods at high temperatures in reducing and oxidising atmospheres.

The electrolyte under consideration in this project was 8 mol% yttria stabilised zirconia (YSZ), approximately 150 μm thick, and intended for operation at 950°C. Although small stacks have run for over a year, very little is known about the mechanical behaviour of the electrolyte under SOFC operating conditions, in particular possible long-term failure processes. This project aimed at investigating these processes, through fast fracture and sub-critical crack growth tests; during the work it was found that creep occurred, and subsequently this was also monitored.

2. Literature and background theory

The limited data on the mechanical performance of 8 mol% YSZ are summarised in this section, as well as a

* Corresponding author at present address: Mechanical Sciences Sector, DERA Farnborough, Hampshire GU14 0LX, UK.

0955-2219/00/$ - see front matter
PII: S0955-2219(99)00080-1

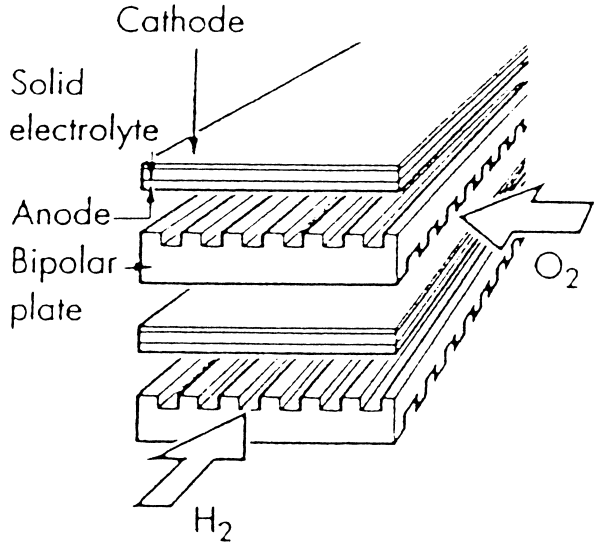

Fig. 1. The configuration of the planar solid oxide fuel cell.[1]

brief outline of the theory behind the experimental techniques used in this work.

2.1. Strength

A flexure test is a convenient form of strength test for a ceramic, and there are several types available. The particular geometry selected for strength tests of the electrolyte samples was the ring-on-ring biaxial flexure, which consists of supporting the sample on a ring, and pushing a smaller, concentrically aligned, ring into it.

The DIN standard[2] for biaxial flexure specifies rig and sample dimensions (such as thickness, t) which ensure that the deflection does not exceed $t/2$ — at which point the strain in the central plane can no longer be considered as zero, and the effect of membrane stresses needs to be taken into account.[3] t is given as 3 mm in the standard, but since in this project actual electrolyte material was to be tested, where $t = 150$ μm, membrane stresses could not be avoided and so had to be quantified. This was done using a finite element analysis (FEA) programme, that enabled the fracture stress to be calculated from failure load, sample dimensions, and Young's modulus, E. Material tape-cast by Kerafol had been tested previously using a ring-on-ring biaxial flexure test at room temperature (RT) and 1000°C.[4] Strength at RT ranged from 156 to 248 MPa, but dropped at 1000°C to 156 MPa, although the latter value was calculated using the RT Young's modulus value (thus the actual strength at 1000°C may have been lower than 156 MPa).

2.2. Sub-critical crack growth

When a component is held under a prolonged load, cracks which are sub-critical, i.e. less than the critical defect size which causes failure, can grow; this is known as sub-critical crack growth (sccg). As soon as the crack reaches critical size, the component fails catastrophically. The time taken for the crack to reach this size is termed the failure lifetime, t_f, and this is required if an assessment of the mechanical performance of the electrolyte during service is to be made.

By assuming that the rate of crack growth follows a power law, failure lifetime can be derived from:[5]

$$\frac{t_f}{t_o} = \left(\frac{\sigma_o}{\sigma}\right)^n \tag{1}$$

where t_o is the failure lifetime at a reference stress σ_o, n is a constant, and σ is the applied stress.

The constant n must be determined experimentally, preferably from samples containing flaws natural to the component; both static and dynamic tests can be used. In a static test, the sample is subject to a constant stress, σ, and the time to failure recorded; $\log(t_f)$ is plotted against $\log(\sigma)$, and n obtained from the gradient in accordance with Eq. (1). In a dynamic test, batches of samples are broken under fast fracture, using different rates of applied stress for each batch. According to Eq. (2), which is an approximation for small stress rates, a plot of log (failure stress, σ_f) versus log (stress rate, $\dot{\sigma}$) will give a straight line of gradient of $1/(1+n)$, from which n can be obtained:[6]

$$\log \sigma_f = \log B + \frac{1}{1+n} \log \dot{\sigma} \tag{2}$$

No previous data for sccg of cubic YSZ was found in literature, but it is known that oxides tend to be more susceptible to sccg in the presence of water, and the rate is also increased at elevated temperatures.[7,8]

2.3. Creep

Creep is the increase in strain with time that a material experiences under prolonged loading. The creep rate, $\dot{\varepsilon}_c$, depends on temperature, T, and applied stress, σ, and is generally described by Eq. (3):[9]

$$\dot{\varepsilon}_c = A\sigma^{n_c} \exp\left[-\frac{Q}{RT}\right] \tag{3}$$

where n_c is the stress exponent for creep, Q is activation energy, R is the universal gas constant, and A is a parameter that depends on the material and test conditions (e.g. oxygen partial pressure in the case of oxides). It is applicable to the steady-state region of creep, and

although originally applied to creep in tension it is now frequently employed with other test modes, such as compression[10–14] and flexure.[15,16] n_c and Q are often found to be a function of temperature and stress; this is usually attributed to changes in deformation mechanisms which are sometimes confirmed by microstructural evidence, as illustrated in the following brief survey of creep of stabilised zirconias.

Creep has been studied in single and polycrystalline samples of YSZ, although at temperatures ($T \geqslant 1400°C$ for the polycrystalline material) higher than those used in the present work. Single crystals with yttria additions of 9.4–21 mol% have been tested over the temperature range 1300–1800°C,[12–14] and a transition in the creep behaviour was observed around 1500°C, irrespective of the yttria content. Below 1500°C there was a high dislocation density, and the dislocations had strongly interacted to give nodes and pinning. It was concluded that the creep was controlled by dislocation viscous glide, with $n_c = 7.3$ and $Q = 714$ kJ/mol. Above this temperature the dislocation density was much lower and dislocation climb dominated, with $n_c = 4.5$ and $Q = 589$ kJ/mol (all values quoted for the crystal containing 9.4 mol% yttria). Creep of 11 mol% YSZ single crystals at lower temperatures (700–1150°C) has been reported;[17] at 700°C, n_c was found to be 318 kJ/mol, which is much lower than the values obtained at higher temperatures.[12–14]

There is a dearth of creep data on polycrystalline yttria-stabilised zirconias. Compression creep tests were carried out on 25 mol% YSZ with grain sizes from 2.5 to 14.5 μm, over the temperature range of 1400–1600°C.[10] The smaller the grain size the faster was the creep rate, and the polycrystalline samples crept at a faster rate than reported for single crystals under the same conditions of stress and temperature. The creep mechanism was considered to be grain boundary diffusion (Nabarro–Herring creep), with n_c and Q determined as 1.2 ± 0.2 and 550 ± 70 kJ/mol, respectively. Ideally $n_c = 1$ for diffusional creep,[18] but n_c values close to unity are usually considered to be consistent with this creep mechanism, e.g. $nc = 0.9_c$ for Al_2O_3–YAG,[11] and $n_c = 1.1-1.3$ for sialon–SiC_W.[16]

Failure of ceramics during creep is usually due to cavitation and/or microcracking associated with grain-boundary sliding; these mechanisms have, for example, been reported in partially stabilised and tetragonal zirconias.[15]

3. Experimental procedure

3.1. Samples

Electrolyte material was provided from two manufacturers, Kerafol and Siemens, in the form of tape-cast discs, approximately 22 mm in diameter and of thickness 150 μm. Some of the Kerafol discs were aged at 950°C for 1000 h.

X-ray diffraction (XRD) was performed using a diffractometer with high temperature facilities on samples from each set from RT up to 1100°C in order to determine the phases present over this temperature range, and one Kerafol disc was analysed using X-ray texture goniometry to see whether the tape-casting process produced an anisotropic microstructure. A scanning electron microscope (SEM) with an energy dispersive analysis of X-rays facility (EDAX) was used to document the microstructure (using gold coated samples), and to measure the yttria content and detect impurities present (using carbon coated samples). DIGIMAPS were also plotted to show the dopant distribution. Grain sizes were measured from SEM photographs of disc surfaces using the linear intercept technique.[19]

Densities were measured using Archimedes' principle. The thermal expansion coefficient of Siemens material was measured with a dilatometer, over the temperature range RT–1000°C. Finally, the surface roughness, Ra, of each side of the discs and the surface profile were recorded using a Talysurf.

Bulk samples, in the form of bars, of nominal dimensions approximately $37 \times 4.5 \times 4.5$ mm were also used in sccg tests. These were manufactured at Imperial College by uniaxially pressing 8 mol% YSZ powder into bars, which were then isostatically pressed at 300 MPa, and sintered at 1500°C for 2 h. The bar surfaces were then ground parallel and the edges bevelled. The grain size, density, and thermal expansion coefficient of the bars were measured as above.

3.2. Strength

The biaxial flexure rig was a standard ring-on-ring type made of silicon nitride. The support ring, of diameter 17 mm, consisted of a circular arrangement of 23 closely spaced polished sapphire balls, and the loading ring, of diameter 3.4 mm, was also made of polished silicon nitride, in order to minimise friction. Fracture strength was determined by loading discs at a rate of 0.5 mm/min and recording the load at failure, which was then inserted into the FEA programme, along with E at the test temperature and sample dimensions. The test conditions for all samples fractured are summarised in Table 1. The strength results were compared using Weibull plots, and fracture faces of broken samples were examined in the SEM.

3.3. Sub-critical crack growth

Both dynamic and static loading tests were performed. For the dynamic technique, bevelled bars were tested at RT at loading rates of 1, 5, 40, 100, 1000 N/min;

Table 1
Numbers of samples and test temperatures used in fast fracture tests

Material		Temperature (°C)	Number of samples
Kerafol	Unaged	RT	15
	Aged	RT	20
	Unaged	950	20
Siemens	Unaged	RT	15
	Unaged	850	5
	Unaged	950	14
	Unaged	1050	5

10 bars were tested at each loading rate. For the static technique discs provided by Kerafol were tested under static loading using the biaxial flexure geometry. Ten support and loading rings were made of alumina, and a furnace adapted so that the support rings remained inside the chamber whilst the loading rings extended to outside the furnace roof; here they were loaded with appropriate weights and, until the sample fractured, they completed individual timer circuits. When a sample failed, this circuit was broken, and hence t_f recorded. Details of the loads and temperatures used during the static tests are given in Table 2.

3.4. Creep

During the sccg tests it was observed that many samples were not fracturing, as had been expected, but deforming plastically. Hence, creep was also monitored over the ranges of stress and temperature given in Table 2, and Q and n_c determined. Strain was calculated from measurements of the sample deformation. Each sample was profiled using the Talysurf over the central region, corresponding to where the alumina loading ring had been positioned. By assuming that the deflection within the equibiaxial stress region (i.e. inside the loading ring) can be considered as part of a sphere, strain, ε can be calculated using Eq. (4):[20]

$$\varepsilon = \frac{4t\delta}{r^2} \tag{4}$$

where t is sample thickness, δ is deflection, and r is the radius of the region under consideration. Strain was converted to strain rate by dividing by the time a test was allowed to run.

A LVDT was also fitted to one sample, which was loaded under 65 MPa at 950°C, in order to monitor the deflection as a function of time.

SEM examination of the fracture faces of broken samples was performed, and the tensile and compressive surfaces also examined. TEM was also employed to compare the microstructure of the plastically deformed samples with those which failed under fast fracture.

Table 2
Loading and temperature conditions used in the sccg and creep tests

Applied stress (MPa)	Temperature (°C)	Time limit[a] (h)	n_f/n_t[b]
46	950	1000	0/10
65	950	1200	1/5
90	950	1200	3/5
103	950	1200	3/5
116	950	1200	1/5
129	950	1200	1/5
145	950	1200	3/3
145	RT	1200	6/6
181	RT	1200	6/6
103	1000	203	1/5
103	975	837	2/5
103	925	1000	1/5

[a] Time limit (h) is defined as the time at which a test was stopped if failure had not previously occurred.

[b] n_f = number of samples which failed within time limit; n_t = number of samples tested.

4. Results

4.1. Samples

The XRD confirmed that the YSZ samples existed in the cubic phase up to and including the maximum temperature employed of 1100°C, and the X-ray texture goniometry result showed that there was no preferred orientation in the microstructure. The amount of yttria measured by EDAX varied from 7.7 mol% in Kerafol to 7 mol% in Siemens' material, as given in Table 3, but no significant amounts of impurity were detected in either set. DIGIMAPS showed that the dopant was uniformly distributed throughout the material.

Density of Kerafol material was lower than that of Siemens, and the grain size was also less, as given in Table 3. The thermal expansion coefficient of tape-cast Siemens material and bulk material was found to be 1.05×10^{-5}/°C over the temperature range RT–1000°C.

There was a difference in the surface finishes of the samples, with both sets of discs having a 'rough' and a 'smooth' surface. In both sets, the 'rough' appeared dimpled and tiny blisters were observed, whereas the 'smooth' surface was grooved on Kerafol samples and flat on the samples from Siemens. The values of roughness are given in Table 3; in all mechanical tests, it was ensured that the 'rough' surface was placed in tension. The surface profile showed that the discs were warped. The warpage was symmetrical around the centre of the discs, and the peak-to-trough values were in the range 26–44 μm.

4.2. Strength

Failure of each sample always originated from the tensile surface and within the region of the loading ring. The Weibull plots showing the RT strength data for the

Table 3
Summary of the structural, physical, and chemical analysis of tape-cast materials, ± one standard deviation

Material		Phase	Mol% yttria	Grain size (μm)	Density (Mg m^{-3})	[a]'Rough' Ra (μm)	'Smooth' Ra (μm)
Kerafol	Unaged	Cubic	7.7	3.6 ± 0.6	5.81 ± 0.10	0.31	0.11[a]
	Aged	Cubic	7.7	3.2 ± 0.4	5.83 ± 0.06	0.29	0.12[a]
Siemens	Unaged	Cubic	7	5.9 ± 0.2	6.08 ± 0.01	0.21	0.09
Bulk	Unaged	Cubic	–	6.9 ± 0.1	5.99 ± 0.01	–	–

[a] Parallel to grooves.

unaged and aged Kerafol samples are shown in Fig. 2, and the RT and 950°C plots for unaged material from the two sources are compared in Fig. 3. The data are summarised in Table 4, where it can be seen that the Kerafol material was stronger than that from Siemens at both RT and 950°C, although strength for both sets decreased at 950°C, by 23% for Kerafol and 30% for Siemens. Using the student *t*-test, with a statistical significance value of 5%, showed that the Weibull modulus for all materials at RT and that for Kerafol at 950°C was the same, but the modulus increased slightly for the

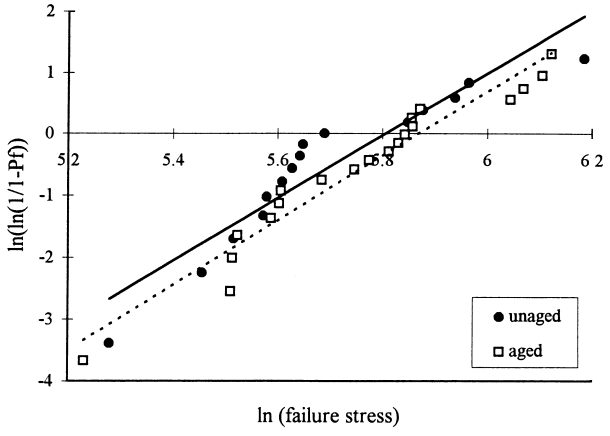

Fig. 2. Comparison of Weibull plots for unaged and aged Kerafol material tested at RT.

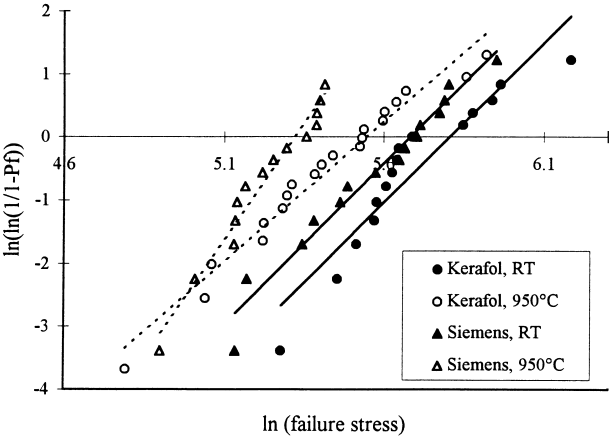

Fig. 3. Comparison of Weibull plots for unaged Kerafol and Siemens material tested at RT and 950°C.

Siemens samples at 950°C. RT strength and scatter of the Kerafol material was unaffected by ageing. The mean strength data for the Siemens samples tested at temperatures up to 1050°C are given in Table 5, which show the values in the temperature range 850–1050°C are considerably less than the RT value; the *t*-test confirmed that the decrement in strength at elevated temperatures was significant. The room temperature and elevated temperature values were superior to those reported by Basu for tape-cast 8 mol% YSZ material.[4]

From the SEM observations, both unaged and aged Kerafol samples failed at RT from porous cavities at, or very close to, the sample surface; these defects ranged from 20 to 60 μm in length, and extended about 20 μm from the surface into the material, as illustrated in Fig. 4. Around this defect site the fracture was transgranular, but the rest of the surface showed evidence of some intergranular failure. Small pores and clusters of pores could be seen throughout the microstructure, as can be seen in Fig. 5.

Some change was noted in the fractography of Kerafol samples fractured at 950°C. Although in some cases failure did initiate from a porous defect, in others there was no obvious defect at the initiation site, as is shown in Fig. 6. Crack propagation across the majority of the

Table 4
Weibull data at RT and 950°C

Material		RT strength, σ (MPa)	RT modulus m	950°C strength, σ (MPa)	950°C modulus m
Kerafol	Unaged	332	5.1	256	4.5
	Aged	353	5.2	–	–
Siemens	Unaged	294	5.1	205	7.3

Table 5
Variation in mean strength, ± one standard deviation, with temperature of Siemens material

Temperature (°C)	Mean strength, σ (MPa)
RT	270 ± 61
850	178 ± 39
950	189 ± 29
1050	214 ± 56

fracture faces was also more intergranular than that at RT. The change in fractography with temperature was more noticeable with the Siemens material. At RT and 850°C, failure of both strong and weak samples was found to have initiated from cavities at, or lying near to, the tensile face. There were less pore clusters than in the samples made by Kerafol, and the crack path was still mostly transgranular across the faces, although tending to be more intergranular at the higher temperature.

At 950°C the failure source was not always a cavity; sometimes there were two or three clearly defined grains surrounded by a completely flat, featureless region. In the samples which did fail from porous defects, individual grains were clearly defined around the edges of the cavities, which had not been seen in samples broken at lower temperatures. Although the grain structure was still transgranular in the vicinity of the defect, it was more intergranular further away.

Of the five samples fractured at 1050°C, only two failed from a porous cavity, where grains were again clearly defined around the edges, as can be seen in Fig. 7. Failure of the remaining samples started from two or three exposed grains in an otherwise completely featureless region, shown in Fig. 8. The majority of the fracture face was now intergranular, with there even being intergranular patches around the initiation sites, as illustrated in Fig. 9.

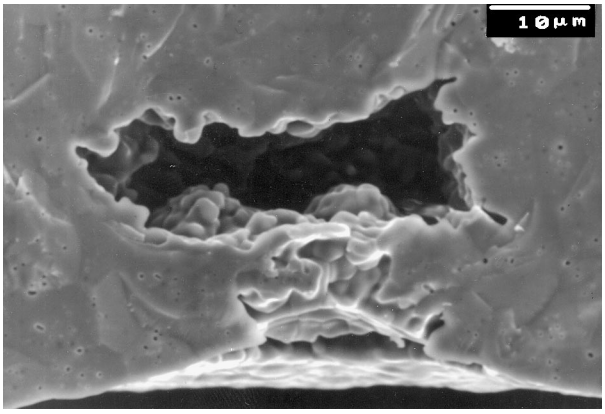

Fig. 4. Typical fracture initiating defect at RT; a porous cavity.

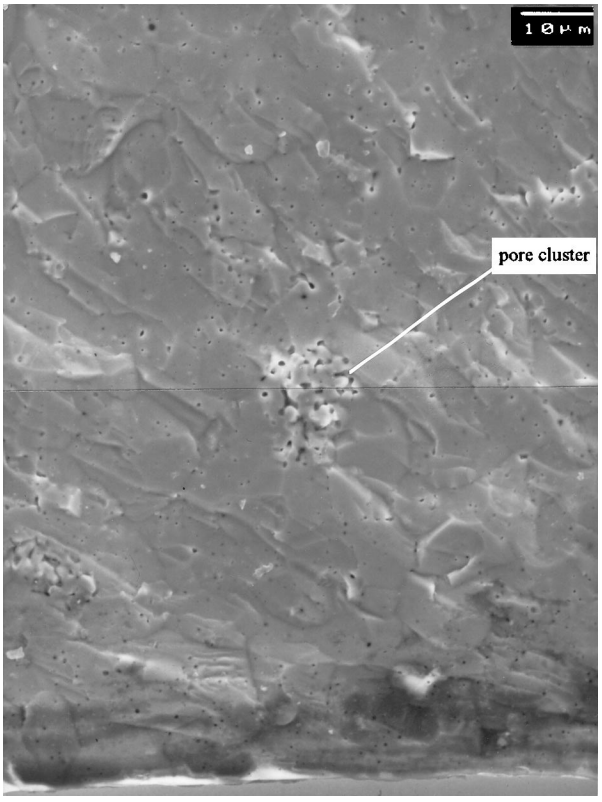

Fig. 5. Illustration of pore clusters seen throughout fracture faces, shown here in a sample of slightly larger grain size than that specified in Table 3.

4.3. Sub-critical crack growth

For bars in dynamic loading tests at RT, the fracture strength increased as the stressing rate increased, as illustrated in the plot of $\log(\sigma_f)$ versus $\log(\dot{\sigma})$, shown in

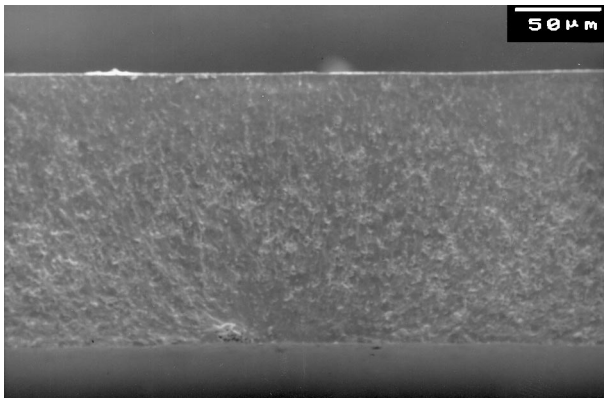

Fig. 6. Fracture face of a Kerafol sample broken at 950°C, showing featureless initiation site.

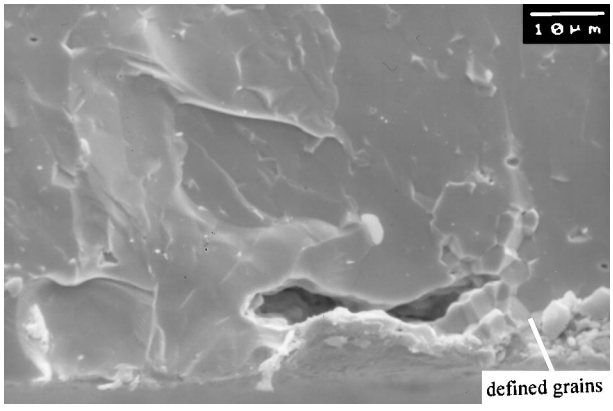

Fig. 7. Failure initiation site of a Siemens sample fractured at 1050°C; a porous defect, with individual grains exposed around the edges of the cavity.

Fig. 10. From the gradient of this plot a value of 11 was calculated for n. SEM examination of fracture faces of the bars showed that failure initiated at the bevelled corners, i.e. from grinding damage, and proceeded in a transgranular fashion. Limited sccg data were collected for the discs tested under static loading, due to samples not failing within the test time limits. The 10 samples loaded under 46 MPa at 950°C survived for 1000 h and so were fractured at RT to see if the period under load at an elevated temperature had affected the material. The test yielded a Weibull strength of 248 MPa and modulus of 4.8; this is a drop of 30% in strength compared with the aged samples, although the scatter is similar. SEM examination showed that fracture initiated from porous defects.

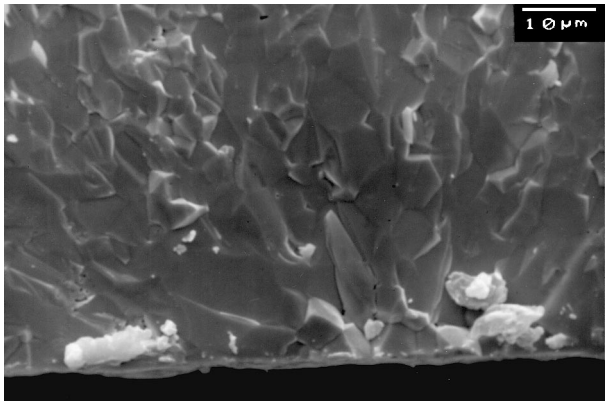

Fig. 8. Fracture face of a Siemens sample broken at 1050°C; failure initiated from two or three grains within a transgranular region, and a mixture of transgranular and intergranular crack propagation.

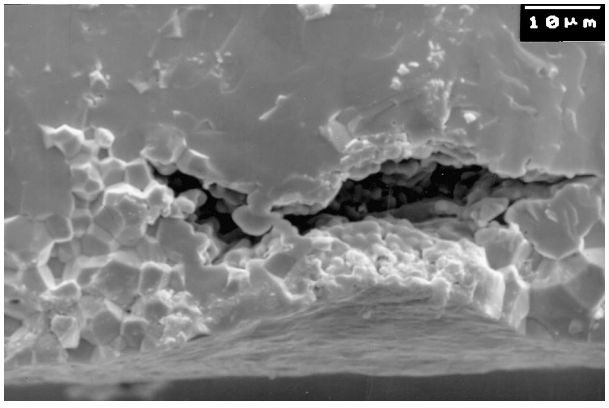

Fig. 9. Failure initiation site of a Siemens sample fractured at 1050°C.

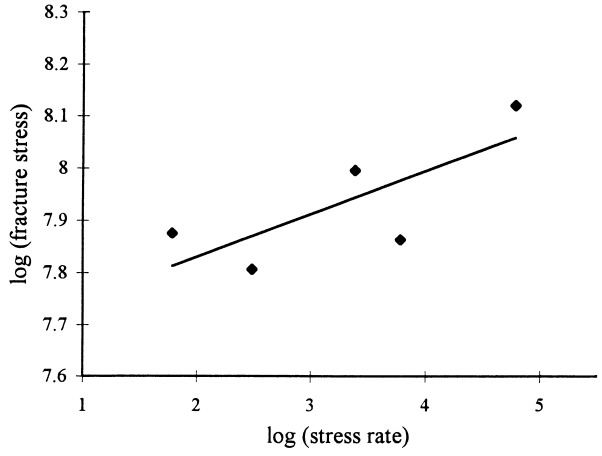

Fig. 10. Plot of log (fracture stress) versus log (stress rate) for bulk samples.

When higher loads were applied to discs it was found that failure would usually occur immediately or within a few minutes, or fracture did not occur and the samples would deform plastically as the test proceeded. The exception to this was at loads 116 and 129 MPa, where one sample did fail under each load after several hours. The results for the static fatigue tests showed that the time to failure decreased as the applied load increased and that the number of samples which fractured increased with increasing applied load. However, overall the number of samples in which significant sub-critical crack growth was observed was limited and hence the evaluation of n using Eq. (1) was not considered appropriate.

SEM examination of the fracture faces showed that for all the discs which failed at RT, under loads of 145 or 181 MPa, the fracture originated from a cavity at the tensile face, within the loading-ring region. At 950°C, samples which failed immediately the load was applied also failed from such porous defects, but for samples which displayed delayed failure at 950°C, the initiation site was found to be featureless, and there was no obvious failure initiating defect.

4.4. Creep

A typical Talysurf profile of a deformed sample is shown in Fig. 11. The creep rates measured are shown in Figs. 12 and 13 as plots of $\ln(\dot{\varepsilon}_c)$ versus $1/T$ and $\log(\dot{\varepsilon}_c)$ versus $\log(\sigma)$. There was good agreement in the strain calculated for samples within each set of conditions, with an error range of 2–11%. Values for n_c and Q calculated from the plots were 0.5 and 320 kJ/mol respectively.

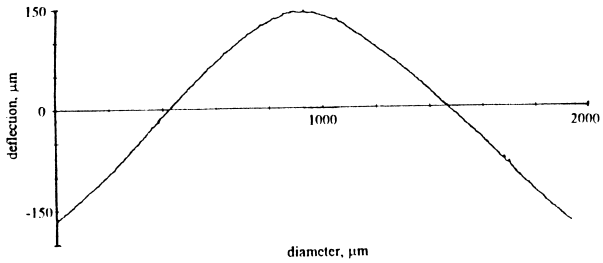

Fig. 11. Typical Talysurf profile of a plastically deformed sample (held under 90 MPa at 950°C for 1200 h).

The deflection with time which was recorded by the LVDT showed that after an initial region where there was very little deflection, a constant deflection rate of 0.2 μm/h was attained. The total deflection recorded by the LVDT was 178 μm, which agreed well with that found from the Talysurf measurement of the profile of the disc (187 μm).

SEM examination of the tensile surfaces of plastically deformed samples showed that the central regions of all the samples appeared 'humped', whereas this was not the case towards the edges of the discs. In addition, for samples held under 90, 116 and 129 MPa there was evidence of cavitation occurring: spherical pores, coalescing to form microcracks, could be seen extending across the surface of the central region, as shown in Fig. 14. Pores and microcracks were also noticed in the samples which had been held under 103 MPa at 1000 and 975°C, but not 925°C. In all the samples examined by SEM the grains were equiaxed in shape — there had been no noticeable grain elongation.

TEM examination did not reveal any dislocations or grain deformation, nor were any secondary phases observed to have precipitated in either aged or plastically deformed samples.

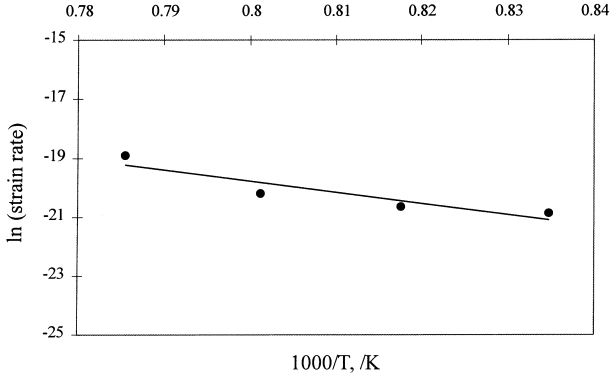

Fig. 12. Plot of ln (strain rate) versus $1/T$ plots for Kerafol discs.

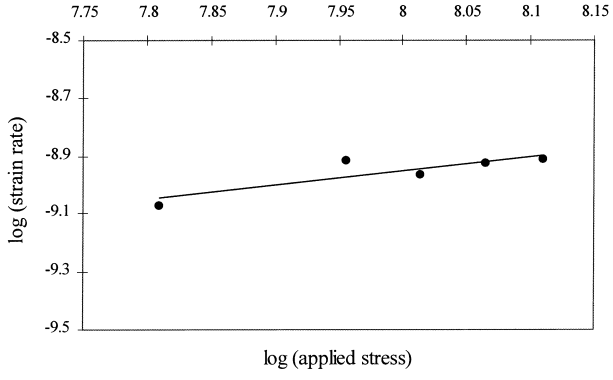

Fig. 13. Plot of log (strain rate) versus log (applied stress) plots for Kerafol discs.

5. Discussion

5.1. Samples

The differences in microstructure of the two sets of samples would be expected in material supplied by different manufacturers. The additional porosity in the Kerafol material is consistent with its lower density, but all the density values were within the accepted range for tape-cast, conventionally sintered, cubic zirconia. Changes in density and grain size due to ageing were so slight that they were considered to be within experimental scatter. The amount of dopant varied by 0.7 mol%, yet the XRD showed both sets existed in the cubic phase through all the experimental conditions, nor was any segregation of the dopant detected on the DIGIMAPS. Thus it can be concluded that the electrolyte material is chemically and physically stable over the temperature range it will experience during service.

The tape-casting process did not produce a microstructure with a preferred orientation, yet would be responsible for surface topography and profile of the discs. The 'smooth' surface of the discs was the side which was in contact with the carrier foil as the tape was cast, and hence reflected the surface finish of this foil. The 'rough' surface had been exposed to air, and it was from this surface that the solvent would evaporate as the tape was dried, and the binder burn out. It is believed that the large porous defects lying on, or close to, this surface formed during these stages, and the pore clusters seen within the microstructure can also be attributed to the initial sintering stages. The fact that Siemens material had less pore clusters may be due to a slower drying rate. It is believed that the warpage is a consequence of the stamping process that was used to produce the discs from the tape-cast sheet, whilst still in the green stage.

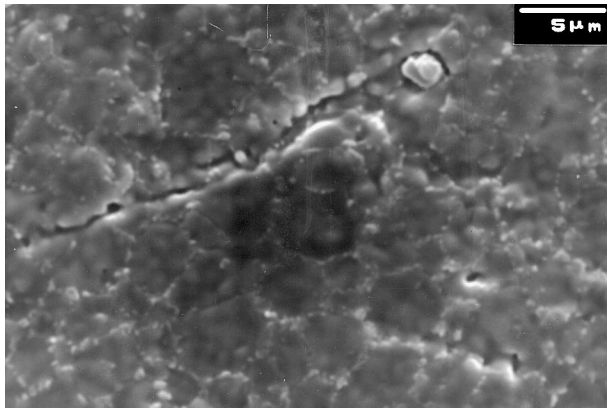

Fig. 14. Pore coalescence in the central region of a sample held under 129 MPa at 950°C.

The bars produced in the laboratory were also cubic phase, with a larger grain size and an intermediate density compared with the discs, and also with a different surface flaw population due to the surface grinding that was used.

5.2. Strength

In a flexure test the failure tends to be dependent on the surface flaws, and this was illustrated in the failure of the discs at RT, with fracture of samples always initiated at porous defects located at the tensile surface within the region of maximum stress. The crack propagation through the Kerafol and Siemens material differed, being more intergranular in the former, and these samples also had a higher strength—both these results could be due to the smaller grain size. The strength and crack propagation process of the Kerafol material was shown to be unaffected by ageing, as would be expected in a material that has been shown to be structurally stable at the temperatures involved.

There was a change in the fast fracture processes at elevated temperatures. The strength of both sets was reduced at 950°C, but only the scatter in the set from Siemens was also reduced (see Table 4). The crack path through the Kerafol samples was still intergranular, but the initiaton site had changed, no longer always being a porous cavity, but sometimes being featureless; this suggests that the defect controlled failure at RT was no longer the only failure process at higher temperatures. The change was more obvious in the Siemens material, since this was examined over a wider temperature range. Although at 850°C the failure initiation and crack propagation processes were similar to those at RT, there seemed to be a mix of processes at 950°C, and by 1050°C they were clearly different: failure was now initiated from individual grains rather than porous cavities, and the crack propagation was intergranular rather than transgranular. It would appear that fracture was proceeding from some kind of flow or grain sliding process, and the drop in scatter, i.e. increase in Weibull modulus to 7.3, confirms that the role of the surface defects was decreasing. A statistical test, the *f*-test (based on the student *t*-test[21]), showed that the slight increase in mean strength on raising the test temperature from 850 to 1050°C (Table 5) was significant, despite the small number of samples tested; this strength increase is attributed to the changes in failure initiation and crack propagation path.

5.3. sccg

The bars tested in dynamic loading exhibited increasing fracture strength with increasing loading rate, since less sccg was able to occur as the load rate increased. Although this test uses natural flaws, it must also be assumed that the same failure mechanisms are followed under all loading rates; this appeared to be the case from the SEM results, where the fracture faces displayed the same initiation and propagation processes. Once again, fast fracture was dominated by the processing stage, this time controlled by surface flaws introduced during grinding. A range of values for n may be obtained for a material, depending on details of the test (method and environment) and material (impurity content and microstructure), e.g. n for alumina is found to range from 20 to 55.[22] Nevertheless, the value of 11 obtained for n in this work is quite low for a ceramic, and suggests, from Eq. (1), that sccg in 8 mol% YSZ will be very dependent on the applied stress.

When loads were applied in the static loading tests, three scenarios occurred. Some samples failed instantly, others after a few minutes delay, and the rest did not fail within the time limit set on the test, as summarised in Table 2. This corresponds to the defect distribution within the samples; immediate failure occurred where there was a critical-sized defect in the vicinity of loading ring, and delayed failure where there was a sub-critical sized defect which grew rapidly to critical size. The trend of lifetime decreasing as applied stress increased again shows the significant effect of stress on the rate of sccg in YSZ, already proved from the low value of n determined in the dynamic loading results. Loading samples at RT prior to testing at 950°C or loading at the test temperature of 950°C did not make any difference to the survival rate when high loads were applied, implying that at high loads sccg dominated over other high temperature processes such as creep.

Samples which did not fracture under static loading went on to deform plastically. It is believed that sccg still occurred in these samples, because of the reduced residual strength found when the 10 discs which had survived being held under 46 MPa for 1000 h at 950°C were fractured at RT, but was either not sufficient to cause failure within the time limit or was inhibited by the creep that also occurred.

The processes of crack propagation in all the samples which did fail under static loading appeared to be the same as in the biaxial fast fracture tests.

5.4. Creep

The constant rate of deflection measured by the LVDT plot indicated that steady state creep was occurring over the majority of the test time, and so Eq. (3) was applicable for calculating the creep parameters. Obviously the creep rate measured would not be independent of stress and time, but since only one sample was monitored using the LVDT the effect of these variables was not investigated by this technique.

It is acknowledged that a flexure test is not the best method of measuring creep, due to the possible

redistribution of stresses as the test proceeds.[6,7] An additional problem with using biaxial flexure was the membrane stresses, since some samples deflected up to twice their thickness. An FEA programme developed at Imperial College[23] enabled the change in stress distribution due to membrane stresses to be calculated and a modified $\log(\dot{\varepsilon}_c)$ versus $\log(\sigma)$ graph was plotted; this showed an increase in the stress exponent, n_c, from 0.5 to 0.7.

The activation energy (320 kJ/mol) and exponent values (0.7) were lower than those previously found at 1400°C.[10] However, TEM examination showed that there were no dislocations present in the material, and the Q value determined is of similar magnitude to that required for lattice cation diffusion in YSZ, 462 kJ/mol,[24] so it was considered that creep was more likely to be occurring by a cation diffusion process than by anion diffusion, which has a much lower activation energy (86 kJ/mol), or by dislocation processes. Since the experimentally determined activation energy was less than that required for self-diffusion of cations through the lattice, and both TEM and SEM examinations showed that the grains were not at all distorted, it is suggested that creep occurred by a grain-boundary diffusion mechanism, where n_c would be approximately 1 as was experimentally determined.

Along the tensile surfaces, the microcracking associated with pore coalescence was only seen in the high stressed regions of samples held at $\geqslant$950°C under high loads. Thus the start of creep rupture was dependent on the stress and temperature experienced.

6. Conclusions

All the materials used in the project were cubic YSZ, with slight variations in microstructure and composition. No structural instability was displayed after ageing at 950°C for 1000 h or heating up to 1100°C in a high temperature diffractometer. The tape-casting process introduced surface defects, which were found to control the initiation of fracture at RT; the strength determined at RT using biaxial flexure ranged from 290 to 350 MPa. At 950°C, the strength decreased, and the processes of crack initiation and propagation had changed, no longer being solely controlled by the processing defects.

Sccg did occur, at both RT and 950°C, and was shown to be very sensitive to the applied stress; an exponent value of 11 was calculated for the bulk samples at RT. At elevated temperatures and low loads, creep was found to occur. A value of approximately 1 was determined for the creep stress exponent, and the activation energy was determined to be 320 kJ/mol; these values, in addition to the microstructural observations, indicated that creep proceeded by a grain-boundary diffusion process.

Acknowledgements

This work was funded by EPSRC and KWU, Siemens. The authors also wish to thank KWU for guidance and advice offered during the project.

References

1. Wersing, W., *Metals and Materials*, 1992, **6**, 326–331.
2. DIN 52 292, 1984.
3. Hearn, E. J., *Mechanics of Materials: An Introduction to the Mechanics of Elastic and Plastic Deformation of Solids and Structural Components*, Vol. 2. 2nd edn. Pergamon, Oxford, 1985.
4. Basu, D., Syskakis, E. 5th IEA workshop, Jülich, Germany, 1993. In *Proceedings of SOFC Materials, Process Engineering and Electrochemistry*, pp. 309–318.
5. Davidge, R. W., McLaren, J. R. and Tappin, G., *J. Materials Science*, 1973, **8**, 1699–1705.
6. Morrell, R., *Handbook of Properties of Technical and Engineering Ceramics. Part 1; An Introduction for the Engineer and Designer*. Her Majesty's Stationery Office, London, 1985.
7. Quinn, G. D., *J. Materials Science*, 1987, **22**, 2309–2318.
8. Liniger, E. G. and Cook, R. F., *J. American Ceramic Society*, 1993, **76**(8), 2123–2126.
9. Evans, R. W. and Wilshire, B., *Introduction to Creep*. The Institute of Materials, 1993.
10. Dimos, D. and Kohlstedt, D. L., *J. American Ceramic Society*, 1987, **70**(8), 531–536.
11. Waku, Y., Nakagawa, N., Wakomoto, T., Ohtsubo, H., Shimizi, K. and Kohtoku, Y., *J. Materials Science*, 1998, **33**, 4943–4951.
12. Martinez-Fernandez, J., Jimenez-Melendo, M., Dominguez-Rodriguez, A. and Heuer, H., *J. American Ceramic Society*, 1990, **73**(8), 2452–2456.
13. Gomez-Garcia, D., Martinez-Fernandez, J., Dominguez-Rodriguez, A., Eveno, P. and Castaing, J., *Acta Materialia*, 1996, **44**(3), 991–999.
14. Gomez-Garcia, D., Martinez-Fernandez, J., Dominguez-Rodriguez, A. and Castaing, J., *J. American Ceramic Society*, 1997, **80**(7), 1668–1772.
15. Chevalier, J., Olagnon, C., Fantozzi, G. and Gros, H., *J. European Ceramic Society*, 1997, **17**, 859–864.
16. Shiogai, T., Tsukamoto, K. and Sashida, N., *J. Materials Science*, 1998, **33**, 769–773.
17. Baufeld, B., Bartsch, M., Messerschmidt, U. and Baither, D., *Acta Metallurgica et Materialia*, 1995, **43**(5), 1925–1933.
18. Ashby, M. F. and Jones, D. R. H., *Engineering Materials Part 1: An Introduction to their Properties and Applications*, 2nd edn. Butterworth and Heinemann, 1996.
19. Anon., *Metals Handbook*, Vols. 8 and 9, 9th edn. American Society for Metals, 1985.
20. Fett, T., Keller, K., Missbach, M., Munz, D. and Pintschovius, L., *J. American Ceramic Society*, 1988, **71**(12), 1046–1049.
21. Miller, J. C. and Miller, J. N., *Statistics for Analytical Chemistry*, 2nd edn. Ellis Harwood Ltd, Halsted Press, 1988.
22. Aeberli, K. E. and Rawlings, R. D., *J. Materials Science Letters*, 1983, **2**, 215–220.
23. Adamson, M., Department of Mechanical Engineering, 1996.
24. Solmon, H., Chaumont, J., Dolin, C. and Monty, C., *Ceramic Transactions, Vol. 24. Point Defects and Related Properties of Ceramics*, ed. T. O. Mason and J. L. Roubert. The American Ceramic Society, 1991, pp. 175–184.